

# Thin-Film Electrode Design for High Volumetric Electrochemical Performance Using Metal Sputtering-Combined Ligand Exchange Layer-by-Layer Assembly

Yongmin Ko, Minseong Kwon, Yongkwon Song, Seung Woo Lee,\* and Jinhan Cho\*

The design of electrode with high volumetric performance in energy storages still remains as a significant challenge because it simultaneously requires a high packing density of active materials for high energy density and a conductive porous structure for facile charge transfer. Here, a novel assembly process is introduced for thin-film anodes for Li-ion battery with a high volumetric energy density and rate performance by systematically controlling the interfacial structure between metal-oxide nanoparticles and/or metal clusters. For this study, oleic-acid-stabilized  $\text{Fe}_3\text{O}_4$  nanoparticles are layer-by-layer assembled with small organic molecules through a ligand exchange reaction, which enable a high packing density. During layer-by-layer deposition, periodic Pt-sputtering onto multilayers significantly reduces the internal resistance of the electrodes but maintains the nanopores formed among the nanoparticles. The resulting anode exhibits an extremely high volumetric capacity of  $\approx 3195 \text{ mA h cm}^{-3}$  and rate performance, which are far superior to that reported for Li-ion battery anodes. Additionally, all components in the electrodes have a stable covalent bond network between the metal atom and the amine group of organic molecule linker, allowing good cycle retention. This approach can be widely applied to the fabrication of various nanoparticle-based electrodes, enabling maximum charge storage performance in confined volumes.

without sacrificing the charge storage rate capability is a key step in achieving a high electrochemical performance with a given electrode volume. To satisfy this issue, it is necessary to realize appropriate porosity and improved electrical conductivity as well as the dense packing of active materials within the electrodes. Metal-oxide nanoparticles (MO NPs) (such as  $\text{MnO}_x$ ,  $\text{SnO}_2$ ,  $\text{MoO}_3$ ,  $\text{CoO}_x$ ,  $\text{Fe}_3\text{O}_4$ , etc.) with high theoretical capacities and large surface areas have been considered as one of the most promising electrode materials for realizing high-performance energy-storage systems including ECs and lithium-ion batteries (LIBs).<sup>[5–11]</sup> For example, when used as an LIB anode,  $\text{Fe}_3\text{O}_4$  has a much higher theoretical capacity ( $\approx 924 \text{ mA h g}^{-1}$ )<sup>[5]</sup> than a commercial graphite anode ( $\approx 372 \text{ mA h g}^{-1}$ )<sup>[12]</sup> due to its reversible, multielectron conversion reaction with lithium (Li) ions.<sup>[7]</sup> Despite their high theoretical capacity, most MO NPs have poor electrical conductivities, which lead to serious issues such as a high internal resistance and insufficient utilization of redox reactions, resulting


in a lower performance than predicted by theoretical values. Therefore, MO NPs should be mixed with conductive materials, such as high-surface area carbon, to increase the electrical conductivity of the electrodes. However, mixing (or blending) of active components with conductive materials and a polymer binder, which is the most common method of preparing electrodes, may still result in a significant internal resistance due to inhomogeneous mixing of the components and the insulating property of the polymer binder. To resolve these issues, 3D conductive matrices composed of soft conductive materials [i.e., carbon nanotubes (CNTs), graphene, conducting polymer, etc.] have been intensively employed as conductive enhancers and/or substrates for MO NP loading.<sup>[13–16]</sup> Although these 3D, conductive networks can improve the specific energy and power performance per unit mass via improved electrical conductivity and effective electrolyte diffusion, their low-density, porous structures can have much difficulty in achieving a high volumetric energy performance. Although the reduction of carbon materials in the MO NP-based electrodes can improve the volumetric energy density due to the increase in electrode density, the reduced rate-performance is still in the dilemma.<sup>[17]</sup>

## 1. Introduction

To meet the growing demands for a variety of integrated, portable microelectronic devices, energy-storage devices such as batteries and electrochemical capacitors (ECs) must generate high-energy and power densities with smaller and thinner electrodes.<sup>[1–4]</sup> Designing electrodes with a high packing density

Dr. Y. Ko, M. Kwon, Y. Song, Prof. J. Cho  
Department of Chemical and Biological Engineering  
Korea University  
145 Anam-ro, Seongbuk-gu, Seoul 02841, Republic of Korea  
E-mail: jinhan71@korea.ac.kr

Dr. Y. Ko, Prof. S. W. Lee  
School of Mechanical Engineering  
Georgia Institute of Technology  
Atlanta, GA 30332-0245, USA  
E-mail: seung.lee@me.gatech.edu

 The ORCID identification number(s) for the author(s) of this article can be found under <https://doi.org/10.1002/adfm.201804926>.

DOI: 10.1002/adfm.201804926

Incorporation of metal NPs into the electrodes as a conductive enhancer can be another way of reducing both the internal resistance and the excess inactive pore volume due to their high electrical conductivity and low volume per mass (i.e., high mass density).<sup>[18–20]</sup> However, for sufficiently fulfilling their role as a conductive enhancer in electrochemical electrodes, the assembly process should ensure the followings: 1) uniform distribution of metal NPs within the whole electrode without the blocking the porous electrode structure, and 2) stable immobilization of metal NPs onto the electrode surface during continuous operation.

Among various approaches for NP-based electrode preparation, layer-by-layer (LbL) assembly using complementary interactions between neighboring components is a versatile, simple, and well-established process that allows tailored thicknesses, compositions, and functionalities.<sup>[21–35]</sup> This approach also enables homogeneous and uniform distribution of active materials in electrodes without undesirable particle agglomeration or segregation, effectively activating the particle functionalities. Furthermore, because the active materials can be directly deposited onto various substrates (or current collectors) without a polymer binder due to their complementary interactions, the interfacial stability between the active materials and the substrate can be significantly enhanced compared to that obtained using a simple blending method. Accordingly, many research groups have attempted to develop LbL-assembled nanocomposite electrodes consisting of high-energy materials and conductive matrices for high-performance energy-storage device applications.<sup>[30–35]</sup> However, the LbL approaches reported to date still have difficulties in significantly enhancing energy density (particularly, volumetric energy density) because of the low mass density of the conductive component. Thus, to achieve the high volumetric energy density, it is essential to develop a new assembly process that can precisely control the connection of energy and conductive materials within a confined volume.

Herein, we report a novel and simple approach for the preparation of thin-film electrodes with exceptional volumetric capacity, improved rate performance, and long-term cycle stability by incorporating metal clusters into the nanovoids formed among LbL-assembled MO NPs. For this study, high-energy Fe<sub>3</sub>O<sub>4</sub> NPs stabilized by oleic acid (OA) were LbL-assembled with small organic molecules [i.e., tris(2-aminoethyl)amine, TREN with  $M_w \approx 146$ ] through a ligand exchange reaction between OA and TREN in organic media. After the ligand exchange reaction, the organic linkers sandwiched between the adjacent Fe<sub>3</sub>O<sub>4</sub> NP layers were small TREN molecules. Therefore, this approach can reduce the interparticle distance between adjacent Fe<sub>3</sub>O<sub>4</sub> NPs, allowing densely packed NP arrays (mass density  $\approx 3.5 \text{ g cm}^{-3}$ ) within a limited volume. Despite the high packing density, the formed NP films possess a nanoporous multilayer structure with porosity of  $\sim 33\%$ , which is reasonable for the facile Li-ion diffusion kinetics within the electrodes.<sup>[36]</sup> Moreover, periodic platinum (Pt) sputtering during the LbL-assembled Fe<sub>3</sub>O<sub>4</sub> NP films significantly reduces the internal resistance of the electrode, and additionally the sputtered Pt nanoclusters have stable covalent bonding with amine-functionalized TREN due to the high affinity between metal and amine groups, while

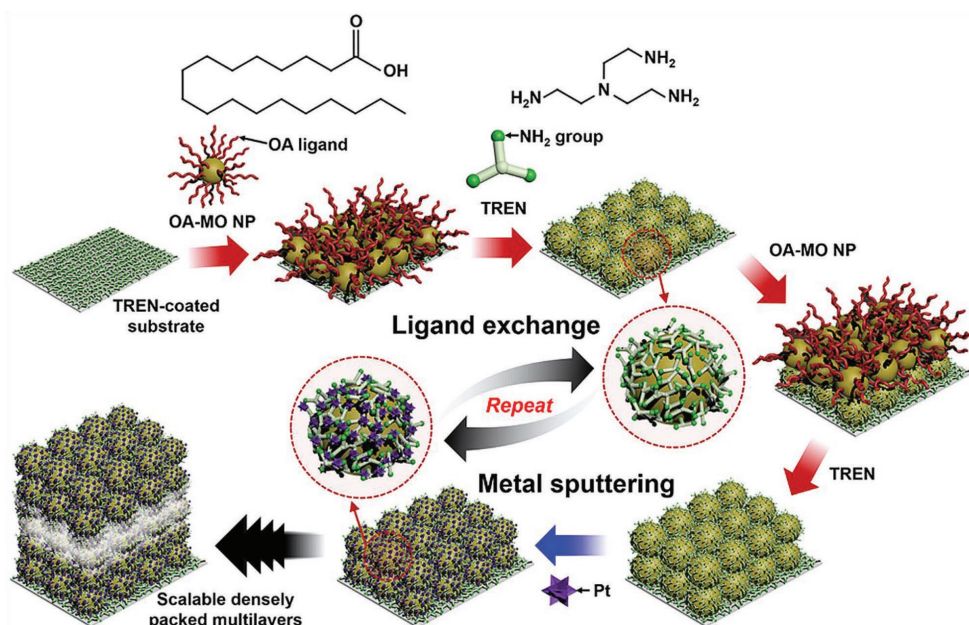
still retaining the nanoporous structure for fast ion diffusion through the electrode. Although high-cost Pt was used as a sputtered metal component for the model system in our study, it should be noted that various metals such as Al, Cu, Au, and Ag showing a high affinity with amine moieties can be also employed for periodic metal implantation instead of Pt. The controlled and repetitive process between LbL assembly and sputtering allowed uniform metal implantation even within few  $\mu\text{m}$  thick LbL film electrodes. Strong interactions between the amine groups of TREN and the introduced Pt allow the uniform distribution of Pt nanoclusters within the multilayer. The Pt-sputtered LbL assemblies of OA-Fe<sub>3</sub>O<sub>4</sub> NP and TREN multilayers [i.e., Pt@(OA-Fe<sub>3</sub>O<sub>4</sub> NP/TREN)<sub>n</sub>] show a remarkable volumetric capacity of  $\approx 3195 \text{ mA h cm}^{-3}$  at a current density of  $470 \text{ mA cm}^{-3}$  for LIB anodes with an excellent rate capability and cycling stability. The introduced approach is a novel strategy to design various energy-storage and energy-conversion electrodes with enhanced volumetric performance.

## 2. Results and Discussion

### 2.1. Preparation and Characterization of Pt-Sputtered Multilayers

First, OA-Fe<sub>3</sub>O<sub>4</sub> NPs 7.5 nm in size with an inverse spinel structure, which was confirmed by high-resolution transmission electron microscopy (HR-TEM) image and X-ray diffraction (XRD) pattern (see Figure S1, Supporting Information), were prepared in toluene (or hexane). These OA-Fe<sub>3</sub>O<sub>4</sub> NPs were LbL-assembled with TREN in ethanol via a ligand exchange reaction between the carboxylate ion (COO<sup>−</sup>) groups of the OA ligands, which have long aliphatic chains, and the amine groups of TREN, which have only six carbon atoms (**Scheme 1**). When the OA-Fe<sub>3</sub>O<sub>4</sub> NP-coated substrate was dipped into the TREN solution [i.e., (OA-Fe<sub>3</sub>O<sub>4</sub> NP/TREN)<sub>1.5</sub>], the characteristic peaks of the OA ligands, such as the C–H stretching peaks in the Fourier transform infrared (FTIR) spectra originating from the long aliphatic chains at 2858 and 2927 cm<sup>−1</sup> and the COO<sup>−</sup> stretching peak at 1412 cm<sup>−1</sup> (see Figure S2, Supporting Information), gradually disappeared as the TREN adsorption time increased (**Figure 1A**). Therefore, alternating TREN and OA-Fe<sub>3</sub>O<sub>4</sub> NPs absorption causes the appearance and disappearance of the characteristic peaks of the OA ligands (at 2858, 2927, and 1412 cm<sup>−1</sup>) when the outermost layer changes from TREN to OA-Fe<sub>3</sub>O<sub>4</sub> NP and *vice versa* (**Figure 1B**). These phenomena imply that only the TREN molecules are simultaneously bound to the upper and lower Fe<sub>3</sub>O<sub>4</sub> NP layers without the presence of bulky insulating OA ligands, which can minimize the distance between the Fe<sub>3</sub>O<sub>4</sub> NPs and notably reduce the internal resistance.

The vertical growth of (OA-Fe<sub>3</sub>O<sub>4</sub> NP/TREN)<sub>n</sub> multilayers was investigated using topographic atomic force microscopy (AFM), UV–vis spectroscopy, and a quartz crystal microbalance (QCM). As the bilayer number (*n*) increased, the film thickness almost regularly increased up to  $\approx 2.12 \mu\text{m}$  with an average thickness of  $\approx 5.9 \pm 0.8 \text{ nm}$  per bilayer (see **Figure 1C** and **Figure S3**, Supporting Information). Notably, the film thickness can easily be increased to the micrometer scale without NP



**Scheme 1.** Schematic illustration of the Pt@(OA-Fe<sub>3</sub>O<sub>4</sub> NP/TREN)<sub>n</sub> multilayers based on the sequential ligand exchange reaction-induced layer-by-layer (LbL) assembly and metal sputtering process.

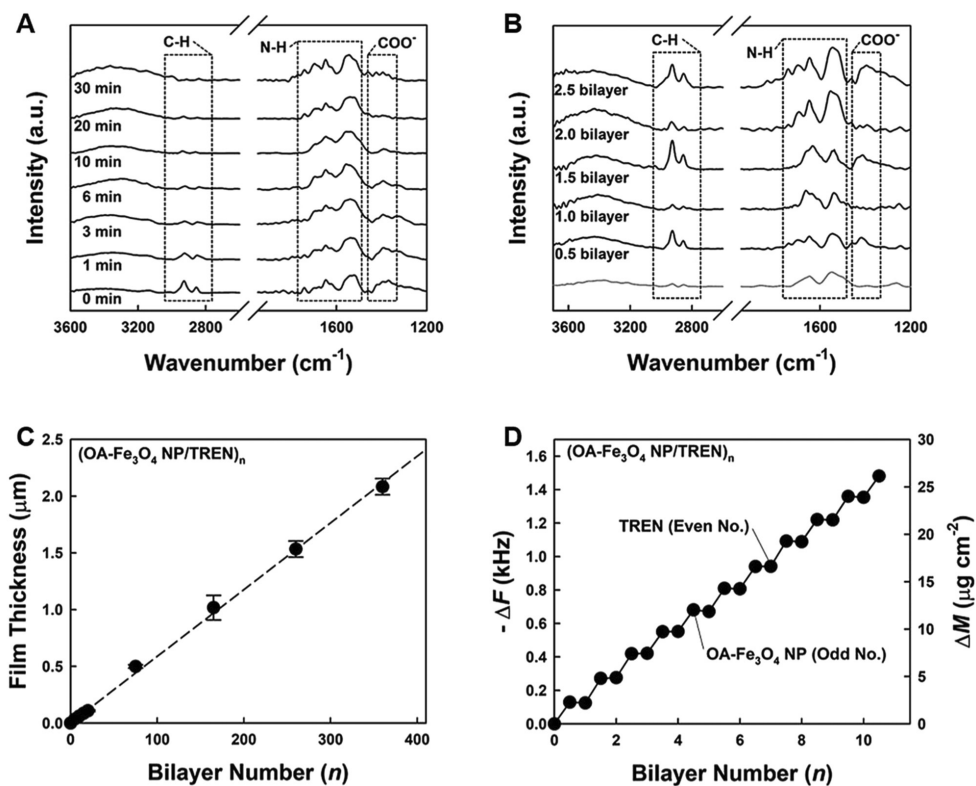


**Figure 1.** Fourier transform infrared (FTIR) spectra of (OA-Fe<sub>3</sub>O<sub>4</sub> NP/TREN)<sub>n</sub> multilayers as a function of the A) bilayer number (*n*) and B) deposit time of TREN onto (OA-Fe<sub>3</sub>O<sub>4</sub> NP/TREN)<sub>1.5</sub> multilayers. The change in COO<sup>-</sup> stretching vibration of OA ligands was monitored using peak at 1412 cm<sup>-1</sup> due to the overlap between the COO<sup>-</sup> stretching peak at 1524 cm<sup>-1</sup> and the N–H bending vibration of TREN. In this case, the COO<sup>-</sup> and C–H stretching peaks originating from OA of Fe<sub>3</sub>O<sub>4</sub> NP gradually disappeared with increasing the deposition time of TREN, while the intensity of N–H bending peak was increased, indicating the ligand exchange behavior between OA and TREN. C) Film thickness variation and D) quartz crystal microbalance (QCM) analysis of (OA-Fe<sub>3</sub>O<sub>4</sub> NP/TREN)<sub>n</sub> multilayers as a function of the bilayer number (*n*).



agglomeration by simply repeating the LbL process, indicating precise and facile control of the film thickness (or mass). The linear increases in the UV-vis absorption spectra and frequency change  $[\Delta F, \text{ (or mass changes, } \Delta M)]$  further imply the regular growth of  $(\text{OA-Fe}_3\text{O}_4 \text{ NP/TREN})_n$  multilayers (see Figure 1D and Figure S4, Supporting Information). In this case, the mass change  $(\Delta M)$  per bilayer ( $n$ ) measured from the alternating deposition of OA-Fe<sub>3</sub>O<sub>4</sub> NP and TREN was  $\approx 2.3 \pm 0.1 \mu\text{g cm}^{-2}$ . In this case, the mass percentage of Fe<sub>3</sub>O<sub>4</sub> NPs in the multilayer film measured to be  $\approx 94.4\%$  by thermogravimetry analysis (TGA) (see Figure S5, Supporting Information), indicating the high packing of Fe<sub>3</sub>O<sub>4</sub> NPs realized by the effective ligand exchange by small molecule linker, TREN, and bulky OA ligands. In addition, the assembled  $(\text{OA-Fe}_3\text{O}_4 \text{ NP/TREN})_n$  multilayers showed a high density of  $\approx 3.5 \text{ g cm}^{-3}$  (density of bulk Fe<sub>3</sub>O<sub>4</sub>  $\approx 5.2 \text{ g cm}^{-3}$ ) with a porosity of  $\approx 33\%$  (see Figure S6, Supporting Information), providing the effective pathway for ion diffusion during continuous electrochemical operation. The optimal pore distribution in the MO-based electrode is a critical design factor to facilitate ion diffusion and buffer the volume change of the active materials, which can maximize the volumetric performance.<sup>[37,38]</sup> The numerous pores of our multilayers formed between the NPs also serve sufficient space for volume change of the Fe<sub>3</sub>O<sub>4</sub> NPs during lithiation/delithiation, resulting in good cycle retention (*more details will be discussed in later part*). To enhance the electrical conductivity of the  $(\text{OA-Fe}_3\text{O}_4 \text{ NP/TREN})_n$  multilayers, Pt was implanted into the nanoporous multilayer films using a metal sputtering process. In typical magnetron sputtering deposition, the metal atoms generated from the target by a magnetic field were adsorbed continuously on the substrate surface, and simultaneously formed nanoclusters through nucleation and growth.<sup>[39,40]</sup> In this case, the penetration depth of sputtered metal atoms is significantly affected by the porosity of initial electrode. When Pt was sputtered on the multilayer films for 30 s, the penetration depth of Pt into the films was  $\approx 20 \text{ nm}$  (Figure 2A–C). Thus, for a uniform distribution of Pt atoms in the thickness direction of multilayer films, the sputtering process must be applied every 3 bilayers of  $(\text{OA-Fe}_3\text{O}_4 \text{ NP/TREN})_3$  ( $\approx 18 \text{ nm}$  in thickness). For example, Pt was sputtered onto  $(\text{OA-Fe}_3\text{O}_4 \text{ NP/TREN})_3$  multilayers for 30 s, and then, 3 bilayers were sequentially deposited on the Pt-sputtered films. This entire process was repeated for

the preparation of  $[(\text{OA-Fe}_3\text{O}_4 \text{ NP/TREN})_3/\text{sputtered Pt}]_m$  with the desired periodic number ( $m$ ) [denoted Pt@ $(\text{OA-Fe}_3\text{O}_4 \text{ NP/TREN})_n$ , where  $n = 3m$ ].

In this case, Pt was uniformly spread from the outer surface of the multilayer film to the inside, showing an increased loading mass of  $\approx 8.3 \mu\text{g cm}^{-2}$  per Pt-sputtering treatment (Figure 3A). Although the mass increased, the increase in the total film thickness and change in the surface morphology were negligible (see Figure 3B and Figure S7, Supporting Information). As a result, the mass density of the multilayers after Pt sputtering was increased up to  $\approx 7.6 \text{ g cm}^{-3}$ . In addition, cross-sectional field-emission scanning electron microscopy (FE-SEM) and elemental mapping showed that the introduced Pt nanoclusters were homogeneously distributed in the OA-Fe<sub>3</sub>O<sub>4</sub> NP/TREN multilayers (Figure 3C). The uniform distribution of the Pt nanoclusters without agglomeration may be due to the high affinity between the Pt atoms and the amine groups of the outermost TREN layer, as confirmed by X-ray photoelectron spectroscopy (XPS) (see Figure 4 and Figure S8, Supporting Information). Wide-survey scan of the OA-Fe<sub>3</sub>O<sub>4</sub> NP/TREN multilayers after Pt sputtering clearly showed the photoemission peaks of Pt along with the peaks from bare OA-Fe<sub>3</sub>O<sub>4</sub> NP/TREN multilayers (see Figure S8, Supporting Information). The high-resolution N 1s spectrum of the Pt@ $(\text{OA-Fe}_3\text{O}_4 \text{ NP/TREN})_{35}$  multilayers showed not only the characteristic peaks of nitrogen-containing species, such as amine/amino (399.4 eV, red dotted line) and oxidic-N (401.8 eV, green dotted line), but also the notable peak at 397.8 eV associated with Pt-N bonding (Figure 4A), which indicated that the sputtered Pt nanoclusters were immobilized in the multilayers through strong amine-metal bonds.<sup>[41,42]</sup> In addition, the Pt 4f<sub>5/2</sub> and 4f<sub>7/2</sub> spin-orbital spectra of the Pt-sputtered multilayers significantly shifted to higher energies, further confirming the formation of stable covalent bonds between the Pt atoms and the amine moieties of TREN (Figure 4B).<sup>[43,44]</sup> In this case, the Pt 4f spectra can be deconvoluted into three Pt oxidation valences of Pt(0), Pt(II), and Pt(IV), which are attributed to the metallic Pt [for Pt(0)] and the surface oxygen linkages by air contact [for Pt(II) and Pt(IV)], respectively.<sup>[42]</sup> In particular, the Pt-sputtered multilayer films [i.e., Pt@ $(\text{OA-Fe}_3\text{O}_4 \text{ NP/TREN})_{35}$ ] showed the larger atomic ratio of Pt(II) species than that of the Pt bulk. This phenomenon can be further demonstrated by the formation

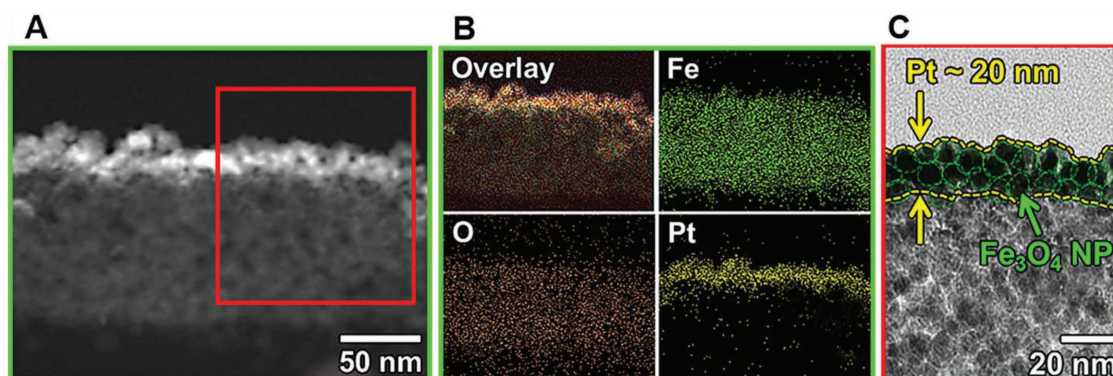


**Figure 2.** A) Cross-sectional transmission electron microscopy (TEM) image, B) energy-disperse X-ray spectroscopy (EDS) elemental mapping images (green solid line), and C) cross-sectional high-resolution transmission electron microscopy (HR-TEM) image of Pt-sputtered  $(\text{OA-Fe}_3\text{O}_4 \text{ NP/TREN})_{20}$  [i.e., Pt@ $(\text{OA-Fe}_3\text{O}_4 \text{ NP/TREN})_{20}$ ] multilayers. In this case, the penetration depth of sputtered Pt (for 30 s) was  $\approx 20 \text{ nm}$ .

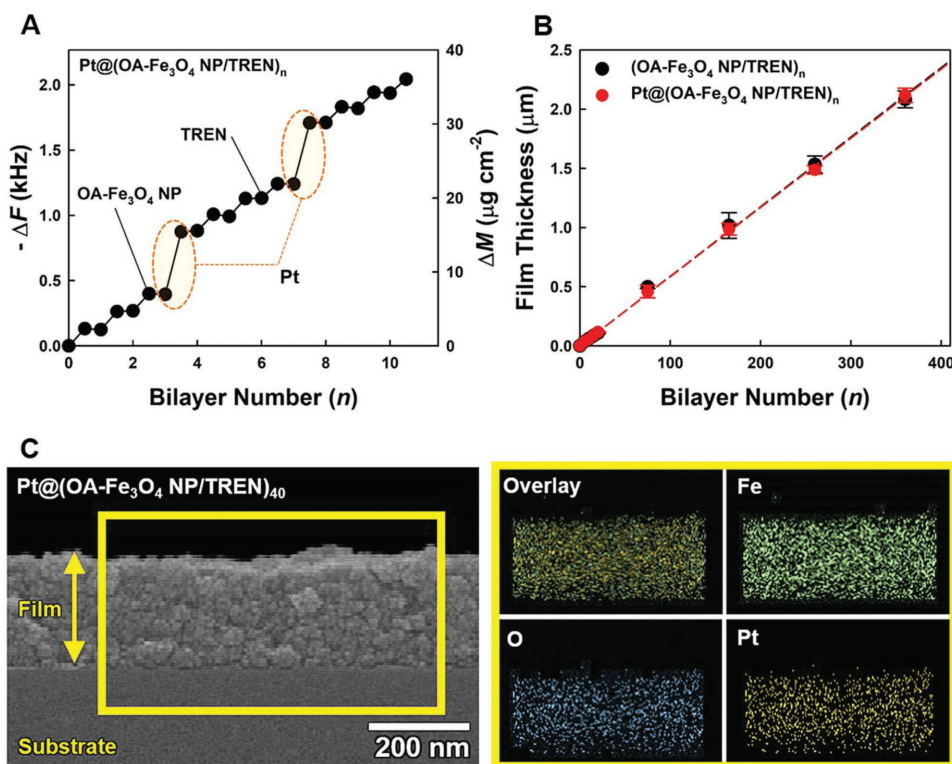


**Figure 3.** A) Quartz crystal microbalance (QCM) data of Pt@(OA-Fe<sub>3</sub>O<sub>4</sub> NP/TREN)<sub>n</sub> multilayers. In this case, the change in frequency ( $\Delta F$ ) and corresponding change in mass ( $\Delta M$ ) after Pt-sputtering were measured as  $\approx 471.4$  Hz and  $8.3 \mu\text{g cm}^{-2}$ , respectively. B) Comparison of bilayer number ( $n$ )-dependent film thickness between (OA-Fe<sub>3</sub>O<sub>4</sub> NP/TREN)<sub>n</sub> and Pt@(OA-Fe<sub>3</sub>O<sub>4</sub> NP/TREN)<sub>n</sub> multilayers. C) Cross-sectional field-emission scanning electron spectroscopy (FE-SEM) images of Pt@(OA-Fe<sub>3</sub>O<sub>4</sub> NP/TREN)<sub>40</sub> multilayers (left) and EDS elemental mapping images (right, yellow region). FE-SEM and EDS images were obtained without pretreatment.

of Pt-N bond caused by the strong interaction between amine moiety of TREN and sputtered Pt.<sup>[45]</sup> Thus, the multilayer films still maintain their nanoporous structure after Pt-sputtering for 30 s (Figure 5A,B). The high-density configuration of the multilayers with numerous nanopores can allow facile ion transport within the interior of the electrodes during electrochemical operations, enabling effective activation of the Fe<sub>3</sub>O<sub>4</sub> NPs. However, a Pt-sputtering time over 30 s caused agglomeration

of the Pt nanoclusters, whose size increased with the sputtering time (Figure 5C,D). After Pt-sputtering for 70 s, the agglomerate size was several tens of nanometers, clogging the nanopores in the multilayers of the Fe<sub>3</sub>O<sub>4</sub> NPs and covering the surface of the film. These phenomena can be further accelerated by the fact that the size (or packing density) of the Pt nanoclusters deposited closer to the surface of the electrode is larger than that of the Pt nanoclusters deposited inside.<sup>[40]</sup> To

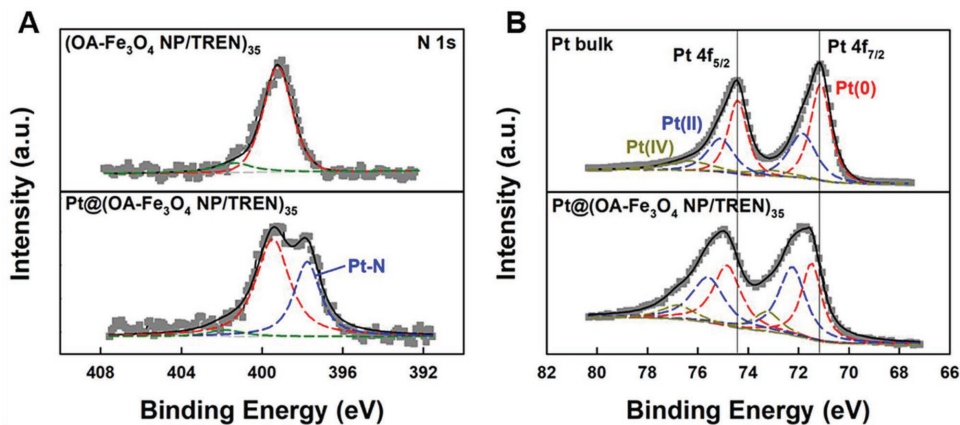


**Figure 4.** A) N 1s XPS spectra of (OA-Fe<sub>3</sub>O<sub>4</sub> NP/TREN)<sub>35</sub> multilayers with and without Pt sputtering. B) Pt 4f XPS spectra of Pt bulk film (prepared by Pt-sputter deposition on a Si-wafer for 100 s, film thickness  $\approx 31$  nm) and Pt@(OA-Fe<sub>3</sub>O<sub>4</sub> NP/TREN)<sub>35</sub> multilayers, respectively.



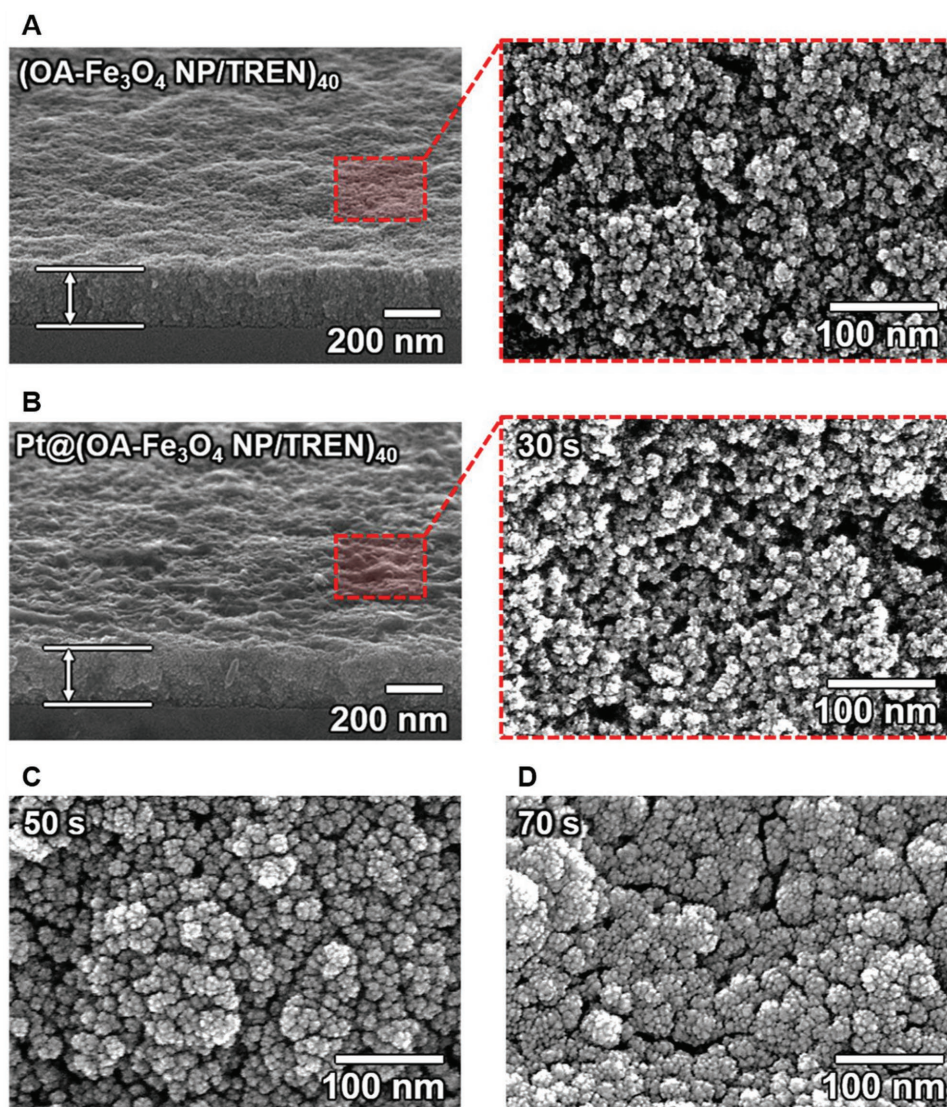


**Figure 5.** Tilted (left) and enlarged planar (right, red-solid box) FE-SEM images of A)  $(\text{OA-Fe}_3\text{O}_4 \text{ NP/TREN})_{40}$  and B)  $\text{Pt}@\text{(OA-Fe}_3\text{O}_4 \text{ NP/TREN)}_{40}$  multilayers with a Pt-sputtering time of 30 s. Planar FE-SEM images of  $\text{Pt}@\text{(OA-Fe}_3\text{O}_4 \text{ NP/TREN)}_{40}$  multilayers after Pt-sputtering for C) 50 s and D) 70 s.

confirm this issue, we investigated the changes in surface morphology of Pt-sputtered multilayer films as a function of the Pt sputtering time (see Figure S9, Supporting Information). With increasing the sputtering time, the root-mean-square (RMS) roughness value tends to increase, indicating that the electrode surface is roughened by the continuous growth of the Pt clusters.

## 2.2. Electrical Property of Pt-Sputtered Multilayers

Based on these results, the electrical properties of the  $(\text{OA-Fe}_3\text{O}_4 \text{ NP/TREN})_n$  multilayers with and without Pt-sputtering were compared (see Figure 6A and Figure S10, Supporting Information). First, the pristine  $\text{OA-Fe}_3\text{O}_4$  NP film with a thickness of  $\approx 0.20 \mu\text{m}$  prepared by a spin-coating process exhibited an extremely low current response level of less than  $\approx 10^{-9}$  mA under an external voltage applied from  $-1.5$  to  $+1.5$  V

(Figure 6A). However, the electrical conductivity of  $(\text{OA-Fe}_3\text{O}_4 \text{ NP/TREN})_{35}$  multilayers with a thickness of  $\approx 0.21 \mu\text{m}$  was  $\approx 1000$  times higher than that of the  $\approx 0.20 \mu\text{m}$  thick pristine  $\text{OA-Fe}_3\text{O}_4$  NP film at an applied voltage of  $\pm 1.5$  V due to the effective removal of insulating and bulky OA ligands through the ligand exchange reaction with TREN. Furthermore, the multilayers with Pt-sputtering [i.e.,  $\text{Pt}@\text{(OA-Fe}_3\text{O}_4 \text{ NP/TREN)}_n$ ] in a thickness range of  $0.45$ – $2.12 \mu\text{m}$  exhibited significantly higher current response levels ( $\approx 10^{-4}$  mA) than the  $(\text{OA-Fe}_3\text{O}_4 \text{ NP/TREN})_{35}$  multilayers without Pt-sputtering ( $\approx 10^{-6}$  mA), which can be explained by the conduction mechanism relation between the current ( $I$ ) and the electric field ( $E$ ) (i.e.,  $I \propto E^\alpha$ ), as shown in Figure 6B. That is, the pristine  $\text{OA-Fe}_3\text{O}_4$  NP film exhibited almost insulating properties with a value of  $\alpha \sim 0.34 \times 10^{-3}$ . However, the electrical conduction behavior of the LbL-assembled films with and without Pt-sputtering followed ohmic law ( $\alpha \sim 1$ ). These results suggest that the bulky OA ligands bound to the surface of  $\text{Fe}_3\text{O}_4$

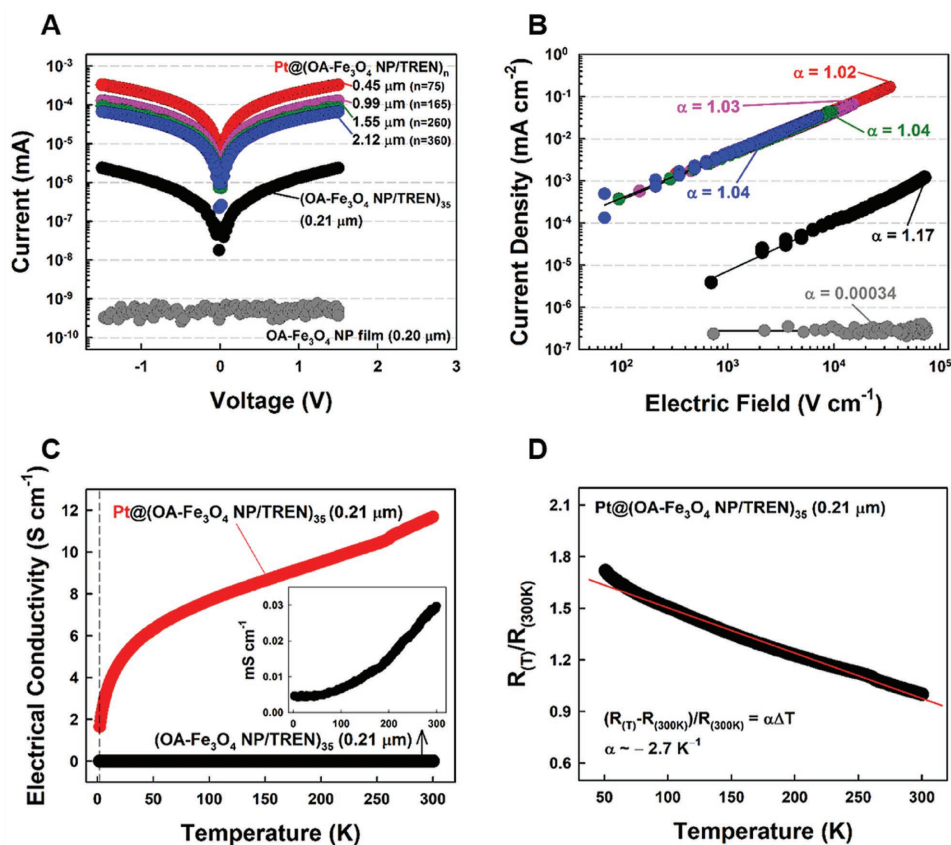


**Figure 6.** A) Current ( $\log I$ )–voltage (V) curves and B) current density ( $\text{mA cm}^{-2}$ )–electric field ( $\text{V cm}^{-1}$ ) profiles of a spin-coated OA- $\text{Fe}_3\text{O}_4$  NP film (thickness  $\approx 20 \mu\text{m}$ ), (OA- $\text{Fe}_3\text{O}_4$  NP/TREN) $_{35}$  (thickness  $\approx 21 \mu\text{m}$ ), and Pt@(OA- $\text{Fe}_3\text{O}_4$  NP/TREN) $_n$  multilayers ( $n = 75, 165, 260,$  and  $360$ ), respectively. C) Temperature (K)-dependent electrical conductivity ( $\sigma$ ) of (OA- $\text{Fe}_3\text{O}_4$  NP/TREN) $_{35}$  and Pt@(OA- $\text{Fe}_3\text{O}_4$  NP/TREN) $_{35}$  multilayers. Inset indicates the enlarged  $K$ – $\sigma$  profile of the (OA- $\text{Fe}_3\text{O}_4$  NP/TREN) $_{35}$  multilayers. D) Plot of temperature (K)-dependent resistance [ $R(T)/R_{(300\text{K})}$ ] for Pt@(OA- $\text{Fe}_3\text{O}_4$  NP/TREN) $_{35}$  multilayers.

NPs play a significant role in lowering the conductivity of pristine OA- $\text{Fe}_3\text{O}_4$  NP films. The electrical conductivity of the Pt@(OA- $\text{Fe}_3\text{O}_4$  NP/TREN) $_{35}$  film with a thickness of  $0.21 \mu\text{m}$  progressively increased as the temperature increased from 2 to 300 K (Figure 6C). As a result, the Pt@(OA- $\text{Fe}_3\text{O}_4$  NP/TREN) $_{35}$  film showed an electrical conductivity of  $\approx 11.6 \text{ S cm}^{-1}$  at 298 K, which is considerably higher than that of the (OA- $\text{Fe}_3\text{O}_4$  NP/TREN) $_{35}$  film with a similar thickness (i.e.,  $\approx 2.8 \times 10^{-5} \text{ S cm}^{-1}$ ) (inset of Figure 6C). In addition, the temperature-dependent resistance [ $R(T)/R_{(300\text{K})}$ ] of the formed Pt@(OA- $\text{Fe}_3\text{O}_4$  NP/TREN) $_{35}$  film shows the typical semiconducting conduction behavior with a negative temperature coefficient of  $-2.7 \times 10^{-3} \text{ K}^{-1}$  determined from the relationship of  $\Delta R/R \propto \alpha \Delta T$  (where  $R$ ,  $T$ , and  $\alpha$  indicate resistance, absolute temperature, and temperature coefficient of resistance) (Figure 6D).<sup>[46]</sup> Based on these results, the introduced Pt was deposited as clusters and not as a continuous phase on the  $\text{Fe}_3\text{O}_4$  NPs due to the strong interactions between the Pt atoms and the amine groups of TREN. Therefore, the electron transport of the electrodes with sputtered and isolated Pt nanocluster follows a tunneling conduction mechanism, which exhibits the linearity between the electrical conductivity ( $\ln \sigma$ ) and temperature ( $K^{-1/2}$ ), instead of metallic conduction behavior (see Figure S11, Supporting Information).<sup>[47]</sup>

### 2.3. Electrochemical Performance of Pt-Sputtered Multilayer Electrodes for LIB Anode

Motivated by the significantly improved electrical conductivity, we evaluated the electrochemical performance of Pt-sputtered (OA- $\text{Fe}_3\text{O}_4$  NP/TREN) $_n$  multilayer electrodes as the anode in LIBs using cyclic voltammetry (CV), galvanostatic charge–discharge (GCD) measurement, and electrochemical impedance spectroscopy (EIS). First, CV tests were performed to clarify the charge-storage mechanism of  $\text{Fe}_3\text{O}_4$  NPs in the potential range of 0.01–3 V versus Li/Li $^+$  at a scan rate of  $0.1 \text{ mV s}^{-1}$  (Figure 7A). The first cathodic sweep of the Pt-sputtered electrode [i.e., Pt@(OA- $\text{Fe}_3\text{O}_4$  NP/TREN) $_{35}$  multilayer] showed two reduction peaks. The first reduction peak at 1.58 V versus Li may be due to the irreversible lithiation of  $\text{Fe}_3\text{O}_4$  NPs [ $\text{Fe}_3\text{O}_4 + x\text{Li}^+ + xe^- \rightarrow \text{Li}_x(\text{Fe}_3\text{O}_4)$  up to  $x = 2$ ], and the second peak at 0.65 V versus Li is ascribed to the subsequent conversion reaction of  $\text{Fe}_3\text{O}_4$  NPs [ $\text{Li}_x(\text{Fe}_3\text{O}_4) + (8-x)\text{Li}^+ + (8-x)e^- \rightarrow 3\text{Fe}^0 + 4\text{Li}_2\text{O}$ ], including the formation of a solid electrolyte interphase (SEI) layer containing  $\text{Li}_2\text{O}$  on the electrode surface resulting from the irreversible decomposition of electrolyte.<sup>[48,49]</sup> The sequential anodic scan displayed a relatively broad peak at  $\approx 1.66 \text{ V}$  versus Li associated with the oxidation of  $\text{Fe}^0$  to  $\text{Fe}^{2+}/\text{Fe}^{3+}$  by the delithiation process.<sup>[50,51]</sup> The characteristic peaks of the lithiation/delithiation



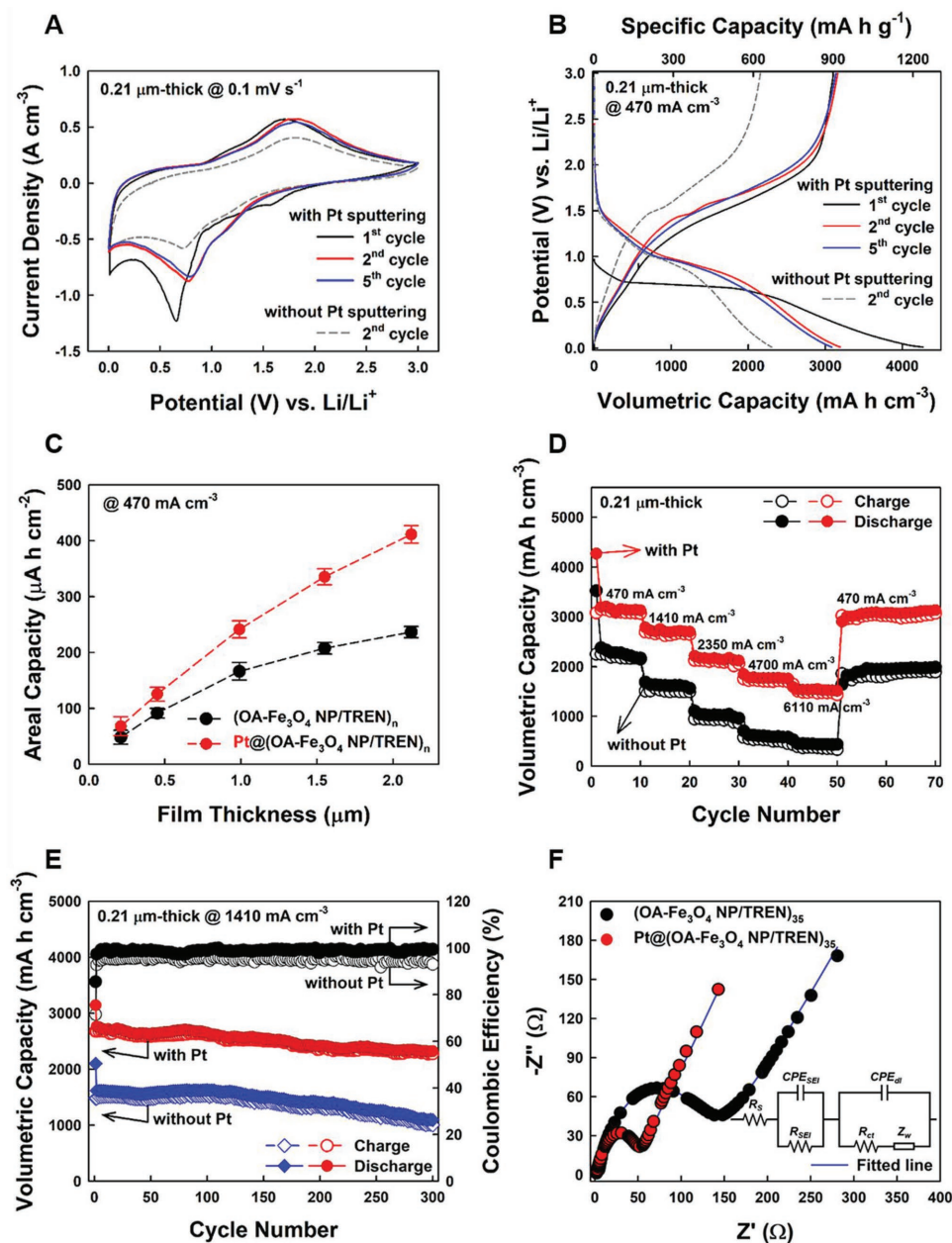


**Figure 7.** Li-ion battery (LIB) anode tests in nonaqueous electrolyte. **A**) CV curves (at a scan rate of  $0.1 \text{ mV s}^{-1}$ ) and **B**) GCD profiles (at a current density of  $470 \text{ mA cm}^{-3}$ ) of  $(\text{OA-Fe}_3\text{O}_4 \text{ NP/TREN})_{35}$  and  $\text{Pt}@(\text{OA-Fe}_3\text{O}_4 \text{ NP/TREN})_{35}$  multilayer electrodes. Comparison of the **C**) areal capacities recorded at a current density of  $470 \text{ mA cm}^{-3}$  for  $(\text{OA-Fe}_3\text{O}_4 \text{ NP/TREN})_n$  and  $\text{Pt}@(\text{OA-Fe}_3\text{O}_4 \text{ NP/TREN})_n$  multilayer electrodes as a function of film thicknesses ranging from 0.21 to 2.12  $\mu\text{m}$ . **D**) Rate capability of  $(\text{OA-Fe}_3\text{O}_4 \text{ NP/TREN})_{35}$  and  $\text{Pt}@(\text{OA-Fe}_3\text{O}_4 \text{ NP/TREN})_{35}$  at varied current densities of 470 to 6110  $\text{mA cm}^{-3}$ . **E**) Cycling retention and coulombic efficiency of  $(\text{OA-Fe}_3\text{O}_4 \text{ NP/TREN})_{35}$  and  $\text{Pt}@(\text{OA-Fe}_3\text{O}_4 \text{ NP/TREN})_{35}$  multilayer electrodes obtained at a current density of  $1410 \text{ mA cm}^{-3}$ . **F**) Nyquist plots of  $(\text{OA-Fe}_3\text{O}_4 \text{ NP/TREN})_{35}$  and  $\text{Pt}@(\text{OA-Fe}_3\text{O}_4 \text{ NP/TREN})_{35}$  multilayer electrodes. The inset indicates the represent equivalent circuit of the multilayer electrodes.

processes shifted to 0.77 V versus Li for the reduction process and 1.81 V versus Li for the oxidation process due to electrode polarization in the second CV scan.<sup>[52]</sup> Upon subsequent CV cycling, the peaks stabilized, indicating the stable lithiation/delithiation behavior of the  $\text{Fe}_3\text{O}_4$  NPs. The Pt-sputtered electrodes showed a higher volumetric current density than the multilayer electrodes without Pt-sputtering at various electrode thicknesses (see Figure S12, Supporting Information), which indicates that

the significantly improved conductivity and reduced internal resistance resulting from Pt-sputtering can improve the charge-storage performance of  $\text{Fe}_3\text{O}_4$  NP-based anodes for LIBs.

GCD measurements were also used to assess the Li-storage performance of the multilayer electrodes (Figure 7B). The capacity drop between the first and second discharging processes resulted from irreversible SEI formation. In the subsequent charge and discharge processes, the potential



plateaus showed the conversion reaction between  $\text{Fe}_3\text{O}_4$  and  $\text{Fe}^0$ , which is consistent with the CV result. Importantly, the Pt-sputtered electrode exhibited a remarkable volumetric capacity of  $\approx 3195 \text{ mA h cm}^{-3}$  at a current density of  $470 \text{ mA cm}^{-3}$ , which was far superior to that of previously reported metal oxide-based anodes ( $785\text{--}2500 \text{ mA h cm}^{-3}$ ) as well as that of the OA- $\text{Fe}_3\text{O}_4$  NP/TREN multilayer electrode without Pt ( $\approx 2305 \text{ mA h cm}^{-3}$ ) (see Figure S13 and Table S1, Supporting Information). The specific capacity of the  $\text{Fe}_3\text{O}_4$  NPs on the Pt-sputtered electrode was  $\approx 913 \text{ mA h g}_{\text{Fe}_3\text{O}_4}^{-1}$ , which is very close to the theoretical capacity of  $\approx 924 \text{ mA h g}^{-1}$  based on the reversible conversion reaction.<sup>[5]</sup> Although the volumetric capacity of the Pt-sputtered electrode gradually decreased with the increasing electrode thickness due to the increase in the internal resistance, the Pt-sputtered electrode maintained a high volumetric capacity of  $\approx 1952 \text{ mA h cm}^{-3}$  at a high thickness of  $\approx 2.12 \mu\text{m}$  ( $\approx 1116 \text{ mA h cm}^{-3}$  for the Pt-free electrode) (see Figure S14A,B, Supporting Information). In addition, the Pt-sputtered electrodes showed a better volumetric capacity retention with the increasing thickness than that showed by the Pt-free electrode (see Figure S14C, Supporting Information). Moreover, the areal capacity of the multilayered electrodes progressively increased with the increasing bilayer number ( $n$ ) (see Figure 7C and Figure S15, Supporting Information). In this case, the areal capacity of the Pt-sputtered electrode was measured to be  $\approx 414 \mu\text{A h cm}^{-2}$  at a thickness of  $\approx 2.12 \mu\text{m}$ , which is almost two times higher than that of Pt-free electrodes ( $\approx 229 \mu\text{A h cm}^{-2}$ ). The obtained areal capacity is suitable for thin-film micro-battery applications,<sup>[53]</sup> and this capacity can be further improved by simply increasing  $n$ . In addition, the increased internal resistance caused by dense packing of MO NPs can be reduced by additional Pt sputtering, so that the resulting multilayer electrodes can exhibit the high volumetric capacity as well as the improved areal capacity. Thus, the areal capacity-to- $n$  relationship for the Pt-sputtered electrode was closer to a linear trend than that of the Pt-free electrodes, offering better scalability. The volumetric capacities of the Pt-sputtered and Pt-free electrodes were evaluated at various current densities (see Figure 7D and Figure S16, Table S2, Supporting Information). As the current density increased from  $470$  to  $6110 \text{ mA cm}^{-3}$ , the volumetric capacity of the Pt-sputtered electrode [i.e., Pt@(OA- $\text{Fe}_3\text{O}_4$  NP/TREN)<sub>35</sub>] decreased from  $3195$  to  $1551 \text{ mA h cm}^{-3}$ , showing a capacity retention of  $48\%$ . On the other hand, the Pt-free electrodes maintained only  $\approx 19.5\%$  of their initial capacity under the same conditions, confirming the critical role of Pt-sputtering on the rate capability for the conversion reaction of  $\text{Fe}_3\text{O}_4$  NPs. When the current density decreased to  $470 \text{ mA cm}^{-3}$  again after 50 cycles, the volumetric capacity of the Pt-sputtered electrode almost recovered up to  $\approx 97.4\%$  of the average capacity recorded in the first 10 cycles (see Table S2, Supporting Information). The Pt-sputtered electrode also displayed a better cycling performance and higher Coulombic efficiency than the Pt-free electrode (Figure 7E). Specifically, the Pt-sputtered electrode maintained  $\approx 84\%$  of the second discharge capacity after 300 cycles at a current density of  $1410 \text{ mA cm}^{-3}$ , which was much better than that of the Pt-free electrode ( $\approx 67.5\%$ ). At the same time, the Pt-sputtered electrode exhibited a Coulombic efficiency of  $\approx 85.5\%$  in the first cycle and a high value of  $>99\%$  after the second cycle, whereas the Pt-free

electrodes showed relatively low values of  $\approx 71.5\%$  and  $\approx 92.9\%$  for the first and subsequent cycles, respectively. These results further emphasize that the Pt-sputtering process can improve not only the overall charge-storage performance but also the cycling stability. In addition to the improved charge diffusion kinetic by incorporation of Pt nanocluster, the sufficient distribution of nanopores in our multilayer electrodes is also an important factor affecting cycling performance as well as facile ion diffusion. To confirm this issue of our multilayer electrodes, we have monitored the volume change against the lithiation-delithiation cycling (see Figure S17, Supporting Information). After the first lithiation process, the apparent volume change was observed with an expansion ratio of  $\approx 185\%$  compared to the initial state. This expanded volume of the electrode was contracted again after the subsequent delithiation process ( $\approx 105\%$ ). In this case, there is no significant change in morphology and total volume as compared with initial state (i.e., before lithiation process), indicating the sufficient pores for buffering the volume change of the NPs and the good reversibility.

Improved electrochemical properties of MO NP-based electrodes after introducing Pt nanocluster can be further confirmed by EIS analysis (Figure 7F). Nyquist plots display representative impedance spectra of OA- $\text{Fe}_3\text{O}_4$  NP/TREN multilayer electrodes with and without Pt sputtering. These spectra composed of series resistance ( $R_s$ , including electrolyte resistance, contact resistance at materials/current collector interface, and intrinsic resistance of electrode materials) at high frequency region (intercept of  $x$ -axis), resistance for SEI formation on the electrode surface ( $R_{\text{SEI}}$ ), charge transfer resistance ( $R_{\text{ct}}$ ) at middle frequency region (semicircular arch), and Warburg impedance ( $Z_w$ ) at low frequency (linear tail). For better understanding, the experimental results were fitted by an equivalent series circuit (the inset of Figure 7F). The Pt@(OA- $\text{Fe}_3\text{O}_4$  NP/TREN)<sub>35</sub> electrode showed  $R_s$  value of  $1.8 \Omega$ , which was much lower than that of the electrodes without Pt ( $4.7 \Omega$ ), implying a decrease in the internal resistance of the active materials by Pt sputtering. Additionally, the  $R_{\text{ct}}$  value of the Pt@(OA- $\text{Fe}_3\text{O}_4$  NP/TREN)<sub>35</sub> electrode ( $52.1 \Omega$ ) was notably lower than that of the Pt-free multilayer electrode ( $143.5 \Omega$ ). These results evidently indicate that the improved electrical conductivity by homogeneously distributed Pt nanocluster within the multilayer electrodes, resulting in better charge transfer kinetics.<sup>[51,54]</sup> Given that various structural properties (i.e., thickness, porosity, and loading amount of the active materials) of the electrodes are almost identical to those of electrodes after Pt sputtering, it is worth noting that the superior electrochemical performance (i.e., volumetric capacity, rate-capability, cycling stability) of the Pt-sputtered electrodes is attributed to the enhanced electrical conductivity by Pt sputtering.

Although Pt was employed as a model system for conductive enhancer, a variety of other metal sources could also be applied to the LbL-assembled electrodes. To confirm this possibility, we further prepared metal-sputtered multilayer electrodes using silver (Ag) and copper (Cu) sputtering and investigated their structures and electrochemical properties (see Figures S18 and S19, Supporting Information). As expected, the sputtered metal (i.e., Ag and Cu) clusters were uniformly distributed throughout the multilayer electrode without segregation (see Figure S18, Supporting Information). As a result, the formed

metal-sputtered multilayer electrodes showed the improved electrochemical performance compared to the metal-free electrodes (see Figure S19, Supporting Information), clearly implying the versatility of our approach.

### 3. Conclusions

We have demonstrated that ultrathin energy-storage electrodes with remarkable volumetric energy-storage performance could be prepared using metal sputtering-assisted LbL assembly. Pt-sputtered Fe<sub>3</sub>O<sub>4</sub> NP multilayers exhibited a high packing density but maintained their nanoporous structure without any agglomerations due to the strong interactions between the amine groups of TREN and the sputtered Pt nanoclusters. This approach significantly improved the volumetric energy density, rate capability, and cycling stability of the Fe<sub>3</sub>O<sub>4</sub> NP electrodes by increasing the electrical conductivity and reducing the internal charge transfer resistance of the total electrode. Furthermore, the Pt-sputtered Fe<sub>3</sub>O<sub>4</sub> NP anode delivered an extremely high volumetric capacity of ≈3195 mA h cm<sup>-3</sup>, outperforming previously reported LIB anodes. Our approach highlights that metal-like conductive pathways can be effectively introduced within the numerous nanopores formed among densely packed MO NPs without a meaningful volumetric increase in the MO NP-based electrode, and as a result, the energy performance (particularly, the volumetric performance) can be maximized in a limited electrode volume. Furthermore, our approach can provide an important foundation for developing and designing high-performance energy-storage devices with ultrathin film structures.

### 4. Experimental Section

**Synthesis of OA-Fe<sub>3</sub>O<sub>4</sub> NPs:** Oleic-acid-stabilized Fe<sub>3</sub>O<sub>4</sub> NP with a diameter of ≈7.5 nm in toluene was prepared as previously reported protocol.<sup>[55]</sup> Briefly, the mixture of Fe(acac)<sub>3</sub> (2 mmol), 1,2-hexadecanediol (10 mmol), oleylamine (6 mmol), oleic acid (5 mmol), and benzyl ether (20 mL) were heated to 200 °C for 2 h under nitrogen flow. Sequentially, the mixture was heated to reflux at 300 °C for 1 h under a blanket nitrogen. The resultant solution was cooled to room temperature and washed with 40 mL of ethanol via centrifugation. Then, black-brown powder was dissolved in toluene in the presence of oleylamine (0.05 mL) and oleic acid (0.05 mL). Centrifugation was applied to remove the undispersed residual. Finally, the product was precipitated with ethanol via centrifugation, and dispersed in toluene.

**Assembly of (OA-Fe<sub>3</sub>O<sub>4</sub> NP/TREN)<sub>n</sub> Multilayers:** The thin-film-type (OA-Fe<sub>3</sub>O<sub>4</sub> NP/TREN) multilayer electrode was prepared using ligand exchange LbL assembly as the model system. The concentrations of TREN and OA-Fe<sub>3</sub>O<sub>4</sub> NPs were adjusted to 1 and 5 mg mL<sup>-1</sup>, respectively. First, the substrates (FTO glass (for three-electrodes tests), a copper plate (for lithium cell tests), Si-wafer, quartz glass, and QCM electrode) that were treated using an UV-ozone cleaner were immersed in a TREN solution for 20 min, and then the TREN-coated substrate was washed using pure ethanol to remove the weakly adsorbed materials. After drying the residual solvent using a gentle flow of N<sub>2</sub>, the substrate was dipped into an OA-Fe<sub>3</sub>O<sub>4</sub> NP solution for 20 min and then washed with pure toluene. This LbL-assembly procedure was repeated until the desired film thickness was obtained. The formed multilayer electrodes were dried at 100 °C under vacuum to remove residual solvent.

**QCM Measurement:** The quantitative analysis of LbL-assembled multilayer film was performed using a quartz crystal microgravimetry

(QCM 200, SRS). The mass change (ΔM) per layer was obtained from the frequency change (ΔF) using the Sauerbrey equation as follows<sup>[56]</sup>

$$\Delta F(\text{Hz}) = -\frac{2F_0^2}{A\sqrt{\rho_q\mu_q}} \times \Delta M \quad (1)$$

where  $F_0$  correspond to the resonant frequency of the fundamental mode of the crystal (5 MHz).  $A$ ,  $\rho_q$ , and  $\mu_q$  indicate the electrode area, density of quartz (2.65 g cm<sup>-3</sup>), and shear modulus quartz (2.95 × 10<sup>11</sup> g cm<sup>-1</sup> s<sup>-1</sup>), respectively. Therefore, these values can be simplified as follows

$$\Delta F(\text{Hz}) = -56.6 \times \Delta M_A \quad (2)$$

where  $\Delta M_A$  is the mass change per unit area (in μg cm<sup>-2</sup>).

**Preparation of Metal-Sputtered Multilayer Films:** Metal (including Pt, Ag, and Cu)-sputtered (OA-Fe<sub>3</sub>O<sub>4</sub> NP/TREN)<sub>n</sub> multilayer films were prepared using an ion sputter-coater (MC1000, Hitachi) with argon (Ar) gas flow under vacuum pressure of ≈10<sup>-2</sup> Torr at a discharge current of 20 mA. For this, Pt was introduced into the as-prepared ≈18 nm thick film electrodes (i.e., three-bilayered multilayer films) by a common metal sputtering deposition technique. Sequentially, OA-Fe<sub>3</sub>O<sub>4</sub> NP and TREN were deposited onto a Pt-sputtered multilayer film using the LbL process mentioned above. After obtaining a film electrode with the desired thickness, the formed electrodes were thermally treated at 100 °C under vacuum for 2 h to eliminate any residual organic solvent.

**Characterization:** FTIR analysis was carried out using a CARY 600 spectrometer (Agilent Technology) in the specular mode at room temperature, and the obtained dataset was plotted after line smoothing using spectra analyzing software (OMNIC, Nicolet). All spectra were obtained from 200 scans. TGA (Q50, TA Instruments) was conducted with increase the temperature from 25 to 600 °C with a heating rate of 5 °C min<sup>-1</sup> under N<sub>2</sub> environment. XPS analysis of the Pt-sputtered OA-Fe<sub>3</sub>O<sub>4</sub> NP/TREN multilayer films was conducted using AXIS-Hsi (KRATOS), and all XPS spectra were calibrated based on the C 1s peak at 284.5 eV from sp<sup>2</sup>-hybridization. Cross-sectional transmission electron microscopy (TEM) of the elemental mapping was performed on a Tecnai F20 operated at 200 kV. The surface morphology and film thickness were monitored by SEM (Hitachi S-4300) and AFM (Park System, XE-100) using the tapping mode. XRD analysis was performed using XRD-2500/PC (Rigaku Co.) with Cu Kα radiation (40 kV, 150 mA). The sample was obtained by drop casting OA-Fe<sub>3</sub>O<sub>4</sub> NPs onto a Si-wafer. The electrical properties were measured in a two-probe method using a semiconductor parametric analyzer (Agilent 4155B) for current–voltage curves with a current compliance of 0.1 mA at room temperature. In this case, a gold wire (diameter ≈ 0.5 mm, Made Lab, Korea) was used as the top and bottom electrodes. The electrical transport mechanism of the formed multilayers was confirmed by a physical property measurement system (PPMS-14, Quantum Design) for temperature-dependent conductivities in a temperature range of 2–300 K. For this experiment, the MO NP-based multilayer films with and without Pt sputtering were deposited on an insulating Si/SiO<sub>2</sub> wafer of 1 × 0.5 cm<sup>2</sup> in size, then silver wires (a diameter ≈ 50 μm, Nilaco Corp.) were contacted and fixed at four different positions on the surface of the multilayer films. After drying the formed samples to remove any residual solvent, these samples were placed in a sealed chamber and the electrical conductivities were measured by in situ monitoring while gradually changing or decreasing the temperature.

**Electrochemical Measurements:** All the electrochemical tests (including CV, GCD measurement, and EIS) were carried out in two- and three-electrode cells using an Ivium-n-Stat (Ivium Technologies, Netherlands) and ZIVE mp2 (Won A Tech. Republic of Korea) with (OA-Fe<sub>3</sub>O<sub>4</sub> NP/TREN)<sub>n</sub> and Pt@(OA-Fe<sub>3</sub>O<sub>4</sub> NP/TREN)<sub>n</sub> multilayer film electrodes as the working electrodes at room temperature. In the three-electrode cell measurements, a platinum wire and 3 M NaCl saturated Ag/AgCl electrode were used as the counter and reference electrodes, respectively. The electrochemical properties of the multilayer-coated FTO electrodes were recorded in the potential range between -0.9 and +0.1 V in a 0.1 M Na<sub>2</sub>SO<sub>3</sub> aqueous solution electrolyte. For the LIB test using

the two-electrode working system, a piece of lithium foil (99.9%, Aldrich) was used as both the counter and reference electrodes in Swagelok-type electrochemical cells (El-cell GmbH, Germany). Furthermore, 1 M LiPF<sub>6</sub> in a mixture of ethylene carbonate/dimethyl carbonate (EC/DMC, 3:7, v/v, Panax Etec Co., Ltd.) was used as the electrolyte. Positive and negative electrodes deposited on copper foil were separated by a Celgard 2325 separator. All battery cells were assembled in an argon-filled glove box (MBraun, O<sub>2</sub> < 0.1 ppm, H<sub>2</sub>O < 0.1 ppm). The electrochemical storage performance of the LIBs was monitored over a potential range of 0.01–3.0 V in the CV and GCD measurements. EIS was performed over a frequency range of 10<sup>5</sup>–0.1 Hz under a perturbation amplitude of 0.01 mV.

## Supporting Information

Supporting Information is available from the Wiley Online Library or from the author.

## Acknowledgements

Y.K. and M.K. contributed equally to this work. This work was supported by the National Research Foundation of Korea grant funded by the Korea government (NRF-2018R1A2A1A05019452; NRF-2018R1A6A3A0101320). The funding statement in the acknowledgements was updated on November 14, 2018, after initial online publication.

## Conflict of Interest

The authors declare no conflict of interest.

## Keywords

layer-by-layer assembly, ligand-exchange reaction, metal sputtering, metal-oxide nanoparticles, volumetric capacity

Received: July 18, 2018

Revised: August 18, 2018

Published online: October 1, 2018

- [1] C. Zhang, W. Lv, Y. Tao, Q.-H. Yang, *Energy Environ. Sci.* **2015**, *8*, 1390.
- [2] M. R. Lukatskaya, O. Mashtalir, C. E. Ren, Y. Dall'Agnese, R. Rosier, P. L. Taberna, M. Naguib, P. Simon, M. W. Barsoum, Y. Gogotsi, *Science* **2013**, *341*, 1502.
- [3] J. Zhou, J. Lian, L. Hou, J. Zhang, H. Gou, M. Xia, Y. Zhao, T. A. Strobel, L. Tao, F. Gao, *Nat. Commun.* **2015**, *6*, 8503.
- [4] X. Yang, C. Cheng, Y. Wang, L. Qiu, D. Li, *Science* **2013**, *341*, 534.
- [5] P. Poizot, S. Laruelle, S. Grugeon, L. Dupont, J.-M. Tarascon, *Nature* **2000**, *407*, 496.
- [6] P. Simon, Y. Gogotsi, *Nat. Mater.* **2008**, *7*, 845.
- [7] S.-H. Yu, S. H. Lee, D. J. Lee, Y.-E. Sung, T. Hyeon, *Small* **2016**, *12*, 2146.
- [8] L. Zhang, H. B. Wu, X. W. Lou, *Adv. Energy Mater.* **2014**, *4*, 1300958.
- [9] P. L. Taberna, S. Mitra, P. Poizot, P. Simon, J.-M. Tarascon, *Nat. Mater.* **2006**, *5*, 567.
- [10] M.-S. Park, G.-X. Wang, Y.-M. Kang, D. Wexler, S.-X. Dou, H.-K. Liu, *Angew. Chem., Int. Ed.* **2007**, *46*, 750.
- [11] T. Brezesinski, J. Wang, S. H. Tolbert, B. Bunn, *Nat. Mater.* **2010**, *9*, 146.
- [12] Y. P. Wu, E. Rahm, R. Holze, *J. Power Sources* **2003**, *114*, 228.
- [13] C. Ban, Z. Wu, D. T. Gillaspie, L. Chen, T. Yan, J. L. Blackburn, A. C. Dillon, *Adv. Mater.* **2010**, *22*, E145.
- [14] Z.-S. Wu, G. Zhou, L.-C. Yin, W. Ren, F. Li, H.-M. Cheng, *Nano Energy* **2012**, *1*, 107.
- [15] S.-M. Paek, E. Yoo, I. Homma, *Nano Lett.* **2009**, *9*, 72.
- [16] Y. Shi, L. Peng, Y. Ding, Y. Zhao, G. Yu, *Chem. Soc. Rev.* **2015**, *44*, 6684.
- [17] Z. Chen, J. R. Dahn, *J. Electrochem. Soc.* **2002**, *149*, A1184.
- [18] C. Kim, J.-W. Jung, K. R. Yoon, D.-Y. Youn, S. Park, I.-D. Kim, *ACS Nano* **2016**, *10*, 11317.
- [19] S. H. Nam, H.-S. Shim, Y.-S. Kim, M. A. Dar, J. G. Kim, W. B. Kim, *ACS Appl. Mater. Interfaces* **2010**, *2*, 2046.
- [20] J. Zhu, Z. Xu, B. Lu, *Nano Energy* **2014**, *7*, 114.
- [21] G. Decher, *Science* **1997**, *277*, 1232.
- [22] J. Cho, K. Char, J.-D. Hong, K.-B. Lee, *Adv. Mater.* **2001**, *13*, 1076.
- [23] F. Caruso, R. A. Caruso, H. Möhwald, *Science* **1998**, *282*, 1111.
- [24] Y. Kim, J. Zhu, B. Yeom, M. D. Prima, Z. Su, J.-G. Kim, S. J. Yoo, C. Uher, N. A. Kotov, *Nature* **2013**, *500*, 59.
- [25] P. T. Hammond, *Adv. Mater.* **2004**, *16*, 1271.
- [26] Y. Ko, H. Baek, Y. Kim, M. Yoon, J. Cho, *ACS Nano* **2013**, *7*, 143.
- [27] Y. Kim, C. Lee, I. Shim, D. Wang, J. Cho, *Adv. Mater.* **2010**, *22*, 5140.
- [28] Y. Ko, Y. Kim, H. Baek, J. Cho, *ACS Nano* **2011**, *5*, 9918.
- [29] I. Cho, H. Jung, B. G. Jeong, J. H. Chang, Y. Kim, K. Char, D. C. Lee, C. Lee, J. Cho, W. K. Bae, *ACS Nano* **2017**, *11*, 684.
- [30] S. W. Lee, N. Yabuuchi, B. M. Gallant, S. Chen, B.-S. Kim, P. T. Hammond, Y. Shao-Horn, *Nat. Nanotechnol.* **2010**, *5*, 531.
- [31] M. Park, Y. Kim, Y. Ko, S. Cheong, S. W. Ryu, J. Cho, *J. Am. Chem. Soc.* **2014**, *136*, 17213.
- [32] L. Peng, X. Peng, B. Liu, C. Wu, Y. Xie, G. Yu, *Nano Lett.* **2013**, *13*, 2151.
- [33] D. Wang, J. Yang, X. Li, D. Geng, R. Li, M. Cai, T.-K. Sham, X. Sun, *Energy Environ. Sci.* **2013**, *6*, 2900.
- [34] Y. Ko, D. Shin, B. Koo, S. W. Lee, W.-S. Yoon, J. Cho, *Nano Energy* **2015**, *12*, 612.
- [35] Y. Ko, M. Kwon, W. K. Bae, B. Lee, S. W. Lee, J. Cho, *Nat. Commun.* **2017**, *8*, 536.
- [36] J. Song, J. Kim, T. Kang, D. Kim, *Sci. Rep.* **2017**, *7*, 42521.
- [37] J. Han, D. Kong, W. Lv, D.-M. Tang, D. Han, X. Zhang, D. Liu, Z. Xiao, X. Zhang, J. Xiao, X. He, F.-C. Hsia, C. Zhang, Y. Tao, D. Goldberg, F. Kang, L. Zhi, Q.-H. Yang, *Nat. Commun.* **2018**, *9*, 402.
- [38] H. Li, Y. Tao, C. Zhang, D. Liu, J. Luo, W. Fan, Y. Xu, Y. Li, C. You, Z.-Z. Pan, M. Ye, Z. Chen, Z. Dong, D.-W. Wang, F. Kang, J. Lu, Q.-H. Yang, *Adv. Energy Mater.* **2018**, *8*, 1703438.
- [39] P. Brault, A. Caillard, C. Charles, R. W. Boswell, D. B. Graves, *Appl. Surf. Sci.* **2012**, *263*, 352.
- [40] A. I. Ayeshe, N. Qamhieh, H. Ghamlouche, S. Thaker, M. El-Shaer, *J. Appl. Phys.* **2010**, *107*, 034317.
- [41] J. Ma, A. Habrioux, Y. Luo, G. Ramos-Sanchez, L. Calvillo, G. Granozzi, P. B. Balbuena, N. Alonso-Vante, *J. Mater. Chem. A* **2015**, *3*, 11891.
- [42] A. Adenier, M. M. Chehimi, I. Gallardo, J. Pinson, N. Vilà, *Langmuir* **2004**, *20*, 8243.
- [43] A. Kumar, H. M. Joshi, A. B. Mandale, R. Srivastava, S. D. Adyanthaya, R. Rasricha, M. Sastry, *J. Chem. Sci.* **2004**, *116*, 293.
- [44] J. Melke, B. Peter, A. Habereeder, H. Ziegler, C. Fasel, A. Nefedov, H. Sezen, C. Wöll, H. Ehrenberg, C. Roth, *ACS Appl. Mater. Interfaces* **2016**, *8*, 82.
- [45] Y. Zhou, T. Holme, J. Berry, T. R. Ohno, D. Ginley, R. O'Hayre, *J. Phys. Chem. C* **2010**, *114*, 506.
- [46] H. Gu, J. Guo, H. Wei, S. Guo, J. Liu, Y. Huang, M. A. Khan, X. Wang, D. P. Young, S. Wei, Z. Guo, *Adv. Mater.* **2015**, *27*, 6277.
- [47] Y. G. Ma, H. J. Liu, C. K. Ong, *Europhys. Lett.* **2006**, *76*, 1144.
- [48] S. K. Behera, *J. Power Sources* **2011**, *196*, 8669.



- [49] Y. H. Kwon, J. J. Park, L. M. Housel, K. Minnici, G. Zhang, S. R. Lee, S. W. Lee, Z. Chen, S. Noda, E. S. Takeuchi, K. J. Takeuchi, A. C. Marschilok, E. Reichmanis, *ACS Nano* **2018**, *12*, 3126.
- [50] Y. Piao, H. S. Kim, Y.-E. Sung, T. Hyeon, *Chem. Commun.* **2010**, *46*, 118.
- [51] C. He, S. Wu, C. Shi, E. Enzuo, J. Li, *ACS Nano* **2013**, *7*, 4459.
- [52] H. Wu, N. Du, J. Wang, H. Zhang, D. Yang, *J. Power Sources* **2014**, *246*, 198.
- [53] N. J. Dudney, *Electrochem. Soc. Interface* **2008**, *17*, 44.
- [54] Y. Yang, X. Ji, M. Jing, H. Hou, Y. Zhu, L. Fang, X. Yang, Q. Chen, C. E. Banks, *J. Mater. Chem. A* **2015**, *3*, 5648.
- [55] S. Sun, H. Zeng, D. B. Robinson, S. Raoux, P. M. Rice, S. X. Wang, G. Li, *J. Am. Chem. Soc.* **2004**, *126*, 273.
- [56] D. A. Buttry, *Advanced in Electroanalytical Chemistry: Applications of the QCM to Electrochemistry*, Marcel Dekker Inc., New York **1991**.